ORIGINAL PAPER

Operational modal analysis, seismic vulnerability assessment and retrofit of a degraded RC bell tower

Simone Castelli[1] · Simone Labò[1] · Andrea Belleri[1] · Babak Moaveni[2]

Abstract

This paper presents damage assessment through Operational Modal Analysis (OMA) and Finite Element (FE) model updating of the bell tower of the church of Castro in Bergamo, Italy. The tower is a 39 m high reinforced concrete structure with hollow cross-section and double-curved shape. The research was dictated by the need to identify the actual damage state of the structure, which was found through visual inspections. Piezoelectric accelerometers were used to record the ambient vibrations in subsequent test setups, using the roving technique for system identification. A detailed FE model was created with shell elements and calibrated to match the system identification results. A simplified beam model was then developed based on the modal analysis results of the detailed model. A sensitivity analysis was performed to identify the most influential model parameters on the modal characteristics of the system. Subsequently, the optimal values of these parameters were determined by an optimisation procedure carried out using a typical global optimization algorithm. The updating results allowed assessment of the actual condition of the bell tower and its seismic vulnerability. Finally, a seismic strengthening solution was recommended.

Keywords Bell tower · Structural damage assessment · Finite element model updating · System identification · Seismic strengthening

1 Introduction

The combination of in-situ testing and computer modelling enables the assessment of the condition of existing structures, in particular by updating the associated finite element (FE) models to match measured data. This process includes data collection, system identification, model definition and model updating [1–13]. Model updating is the process of tuning uncertain model parameters to minimise the error between features derived from measured data and those estimated by the mathematical model. Common features used for model updating are the natural frequencies and mode shapes, which can be derived from both vibration measurements and dynamic models [14–16]. Ambient vibration measurements are often used to identify the dynamic

properties of buildings. The process of identifying modal parameters (natural frequencies, damping ratios, and mode shapes) from ambient vibration measurements is referred to as operational modal analysis, as the measurements are collected during the normal operation of building systems.

This paper presents the OMA, model updating, seismic assessment and retrofit of the bell tower of the church of San Giacomo (Fig. 1) in the city of Castro (Bergamo—Italy). The bell tower is 39 m high and has a hollow reinforced concrete (RC) cross-section and a double-curved shape. The tower was designed by the architect Vittorio Sonzogni in 1966 and built in 1969 together with the adjacent church.

The aim of the work is to verify and quantify the damage to the structure to assess a possible damage propagation due to the bell's vibrations and to define a representative FE model for an accurate seismic assessment of the tower. This process is carried out through a modal identification of the structure to estimate its natural frequencies and mode shapes. Then, a FE model updating was performed through an optimisation procedure that starts from a sensitivity analysis to find the most influential model parameters on the modal properties of the system. In this work, model updating

✉ Andrea Belleri
andrea.belleri@unibg.it

1 Department of Engineering and Applied Sciences, University of Bergamo, Bergamo, Italy

2 Department of Civil and Environmental Engineering, Tufts University, Medford, USA

Fig. 1 a View of the church with the adjacent bell tower; **b** bell tower at the time of construction
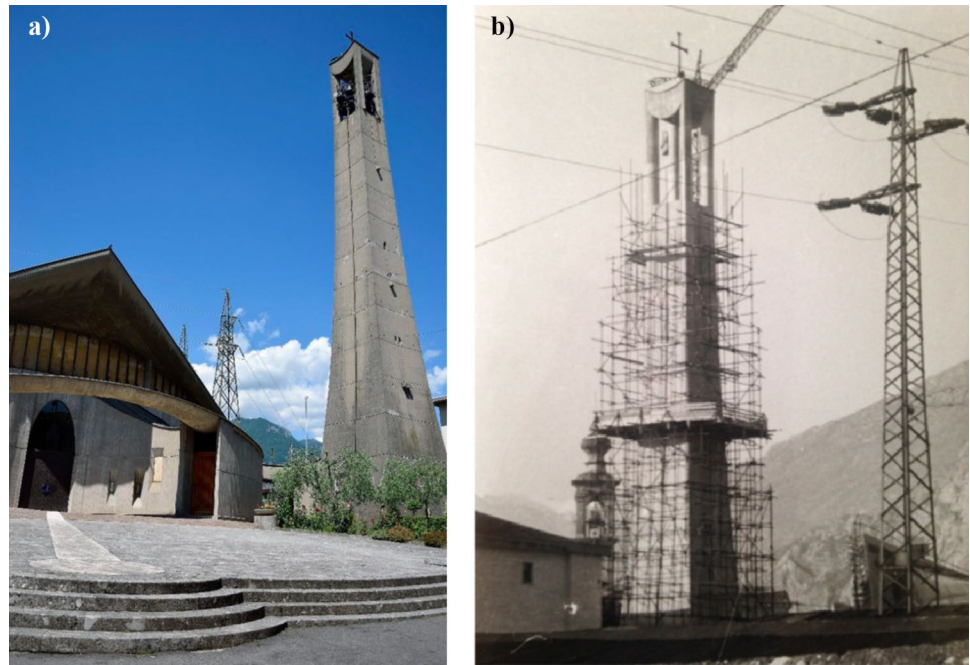
was performed in a deterministic approach through local optimisation. Once the model was calibrated, the seismic vulnerability of the structure was assessed and efficient strengthening solutions were recommended.

2 Bell tower of the church of castro

2.1 Architectural aspects

The almost 39 m high RC bell tower (Fig. 1) has an internal square cross-section with a plan curvature on the four sides and a curvature along the height (Fig. 2). The bell tower extends over seven levels above ground and one below ground. The floors consist of 20–25 cm thick RC slabs. On the top floor is the belfry with a height of 9.30 m, a square cross-section of (2.81×2.81) m^2 and vertical openings of (1.56×4.84) m^2 on the four sides. The weight of the bells was estimated at 2 kN/g. The main geometric details are shown in Fig. 2. Noteworthy is the presence of a continuous vertical discontinuity on two opposite sides of the bell tower. Figure 3 shows an example of the original documentation.

2.2 On-site survey

The bell tower was in an evident state of deterioration (Fig. 4), with a horizontal wide crack at the 3rd level, probably due to several factors, such as the curvature of the cross-section, which is more pronounced at this level, and the vertical curvature, which results in a marked washing out of the concrete, highlighted by the chromatic

surface change. In addition, the vertical openings and the horizontal joints collect a greater amount of rainwater that penetrates from above, leading to significant deterioration of the tower, such as corrosion of the rebars, exacerbated by the presence of chemical substances due to previous pickling operations in a nearby steel factory. Gravel pockets on the surfaces caused by faulty execution of the concrete pour were also noted, as well as spalling of the concrete cover at the corroded reinforcement areas. Some relevant details are shown in Fig. 4.

The carbonation front was measured by testing core samples taken from the 1st level of the bell tower and concrete powders collected from boreholes at different levels. The carbonation front reaches up to 88 mm on the inner sides, while it is 64 mm on the outer sides. Since the concrete cover is between 30 and 50 mm on both the inside and outside, carbonation has thus clearly reached the reinforcing steels, favouring their corrosion and consequent spalling of the concrete cover. As for the mechanical strength of the concrete, four concrete cores were taken on the 1st level and then tested. The average strength of the cylindrical specimens is approximately 24.5 MPa, which is consistent with the concrete used at that time.

The possible extension of damage due to daily vibrations was also investigated during the on-site survey. On-site measurements were taken near the damaged region on the 3rd level to monitor the ambient vibrations, especially during the bells celebrating in both hammer mode and swinging mode. The instrumentation used consisted of low-noise mems accelerometers (AX-3D XRange, manufactured by BeanAir) and measurements were taken at an acquisition
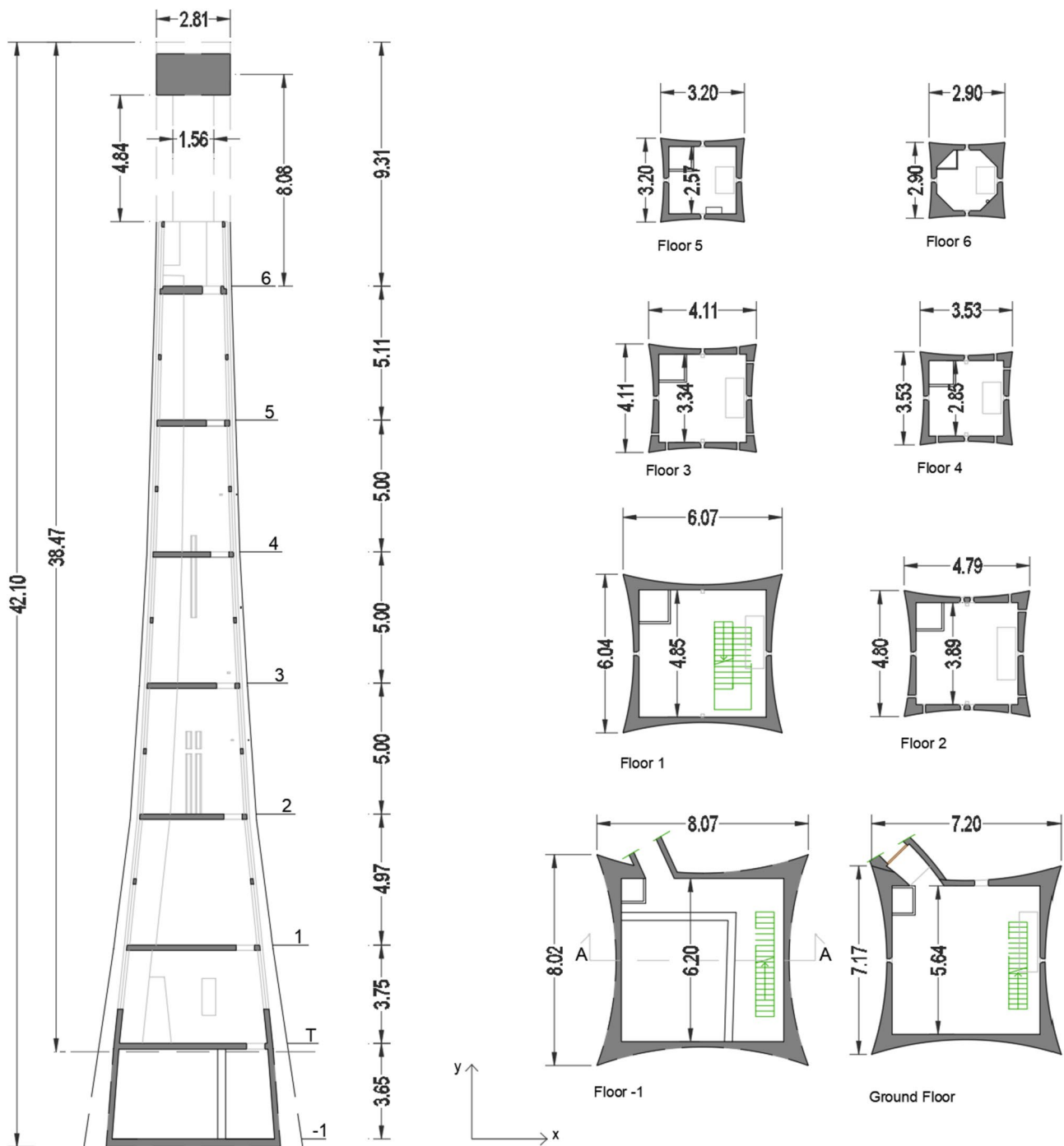
Fig. 2 Vertical and horizontal cross-sections of the bell tower at the various levels. *Note*: Dimensions in meters

frequency of 100 Hz; the recorded data was digitally filtered with a band-pass filter in the range 0.2–50 Hz.

Damage caused by vibration is usually assessed by measuring the particle velocity or uniaxial velocity of a given region [17], as this kinematic quantity is directly related to kinetic energy (Fig. 5). The velocity was determined from the integration of the acceleration measurement and by applying the same digital filter used to cleanse the raw data. The determined particle velocity was at the limit of incipient non-structural damage, especially in the case of bell oscillation. Considering the state of the structure (oxidation of reinforcing bars and concrete spalling), the recorded vibrations, even if they do not cause structural problems in new constructions, could accelerate the degradation process by
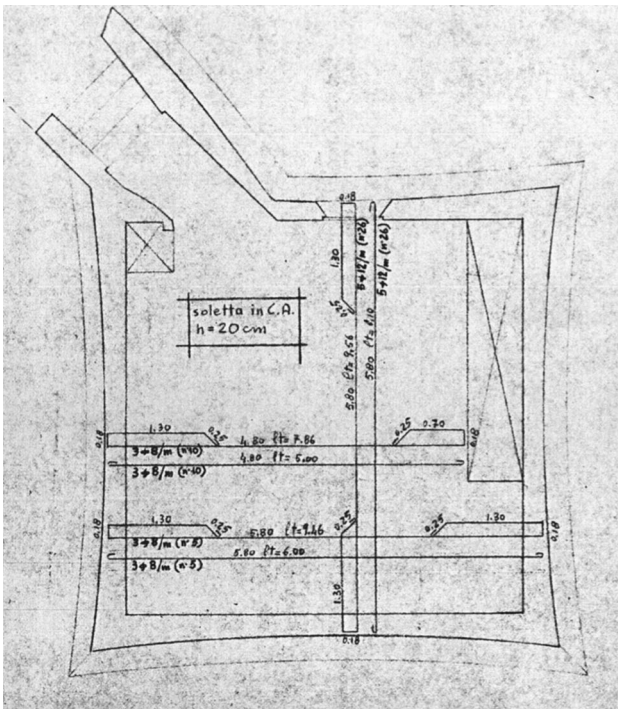
Fig. 3 Example of the original drawings of the bell tower: steel reinforcing bars details for the ground floor

increasing the propagation of cracks and favouring concrete spalling.

3 System identification

The Frequency Domain Decomposition (FDD) algorithm [18] was selected for the operational modal analysis of the bell tower. Frequency Domain approaches are based on time-correlated signal processing through a Discrete Fourier Transform (DFT). FDD method performs a Singular Value Decomposition (SVD) of the cross power spectral density matrix at each frequency. This procedure separates noisy data from disturbances of various sources and appears able to pick up closely spaced modes by considering more than one singular value. Typical underlying hypotheses of FDD methods are broadband ambient excitation and geometrically orthogonal mode shapes of close modes.

$$G_{yy}(\omega) = \overline{H}(\omega)G_{xx}(\omega)H^{\mathrm{T}}(\omega) = \cdots = \overline{\Phi}\left\{ \mathrm{diag}\left[\Re e\left(\frac{2d_k}{\mathrm{i}\omega - \lambda_k} \right) \right] \right\} \Phi^{\mathrm{T}} \tag{1}$$

In the above equation, $G_{xx}(\omega) \in \mathbb{R}^{r \times r}$ is the Power Spectral Density (PSD) matrix of the input load, r is the number of inputs, $G_{yy}(\omega) \in \mathbb{R}^{m \times m}$ is the PSD output matrix, where m is the number of output channels (responses or measurements), $H(\omega) \in \mathbb{R}^{m \times r}$ is the Frequency Response Function (FRF) matrix. The overbar denotes complex conjugate and the apex T the transpose, $\lambda_k = -\zeta_k\omega_k + \mathrm{i}\omega_{dk}$ is the system eigenvalue with $\omega_{dk} = \omega_k\sqrt{1-\zeta_k^2}$ and ω_k is the natural frequency, and ξ_k is the damping ratio, $d_k = \Gamma_k^H G_{xx}\Gamma_k/(2\zeta_k\omega_k)$
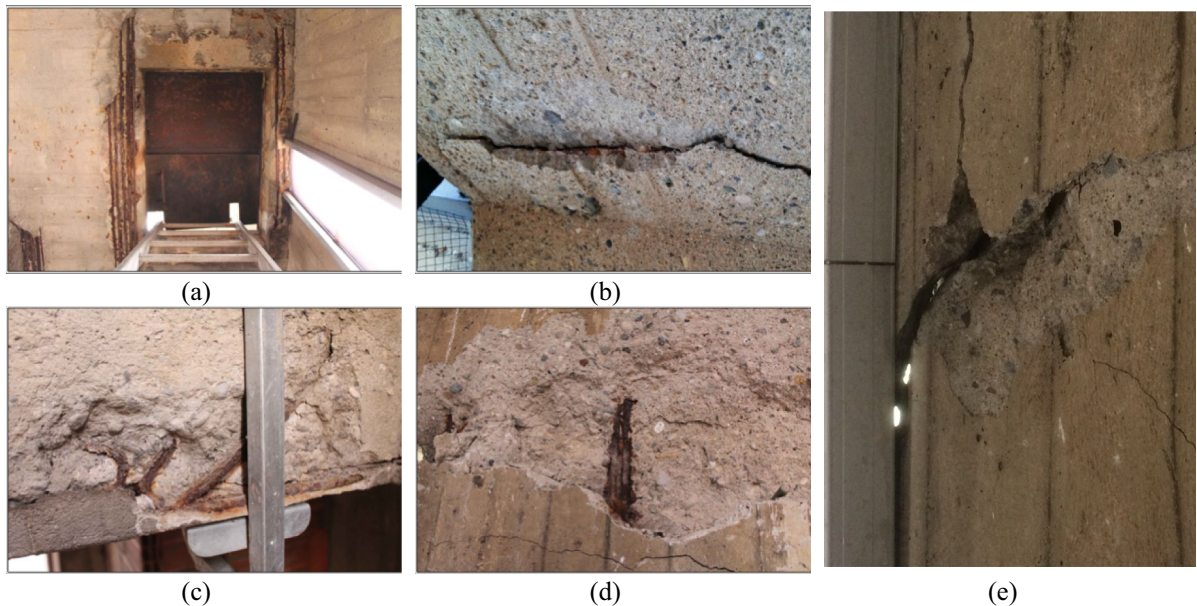

Fig. 4 Details of some deteriorated areas of the bell tower: **a** last floor; **b** belfry; **c** 5th floor slab; **d** 3rd floor slab; **e** cracking at the 3rd level
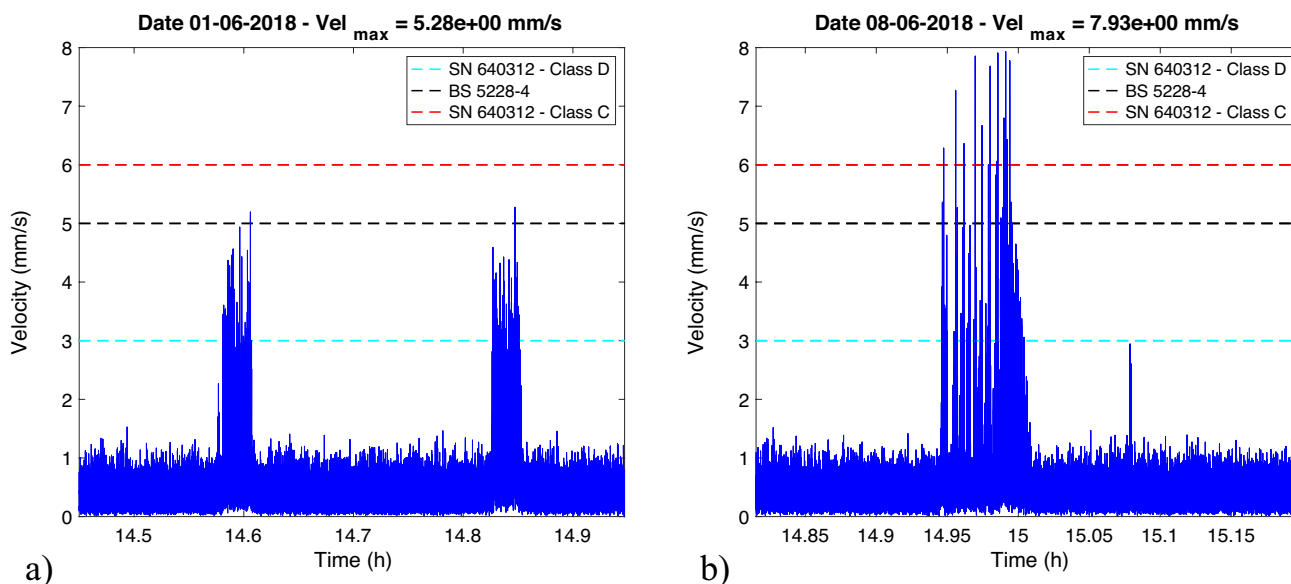
Fig. 5 Particle velocity at the damaged region of the 3rd level during bells in celebration with hammers (**a**) and bells swinging (**b**)
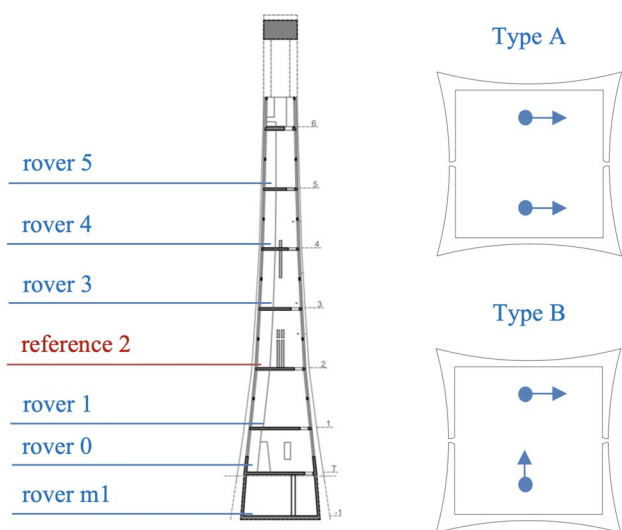

Fig. 6 Ambient vibration recording setup

is a scalar, and $\mathbf{\Phi}$ is the eigenvector matrix, gathering the *n* eigenvectors ϕ_i as columns which correspond to the mode shapes. The matrix in Eq. 1 is decomposed using a SVD technique into a set of singular values and singular vectors. From the former, natural frequencies are extracted; from the latter, approximate mode shapes are obtained.

Four highly sensitive piezoelectric accelerometers (Wilcoxon 731A) in two different configurations (Type A and Type B) were placed for system identification (see Fig. 6). To overcome the limited availability of sensors, the roving technique was used. Specifically, in each configuration, two sensors were left in the same position for all registrations

(reference), while the others were moved for each registration (rover). The Type A configuration allows the identification of possible torsions in each plane, while the Type B configuration allows the estimation of modal shapes in the orthogonal direction. Overall, despite the limited availability of sensors, the roving technique allowed a comprehensive assessment of the system's behavior. The data were processed using a band-pass filter in the range 0.2–40 Hz. The various acquisitions have variable lengths between 250 and 600 s, which have been found proven to be sufficient for identifying the system.

Figure 7 shows an example of the FDD results. The 1st peak was discarded because it corresponded to a local vibration mode. It is worth noting that the first two frequencies are very close and could only be identified by careful choice of frequency resolution (Fig. 7a). As an example, Fig. 7b shows the polar plot of the 3rd vibration mode shape in complex plane. From the figure the eigenvector components are practically collinear, i.e., mainly represented by real numbers, which indicates that the vibration mode is classically damped.

Once the modal identification of each record was completed, a statistical analysis of the estimated frequencies was performed. The results of the identification are presented in Table 1 in the form of estimated frequencies.

Figure 8 shows the boxplots of the results plotted according to the corresponding distribution curve. The boxes are defined by the 25th and 75th percentiles, while the middle markers represent the median values. The whiskers represent the maximum and minimum values without considering outliers. Outliers are plotted individually with the symbol '+'. From the results (Table 1 and Fig. 8), there is little variance
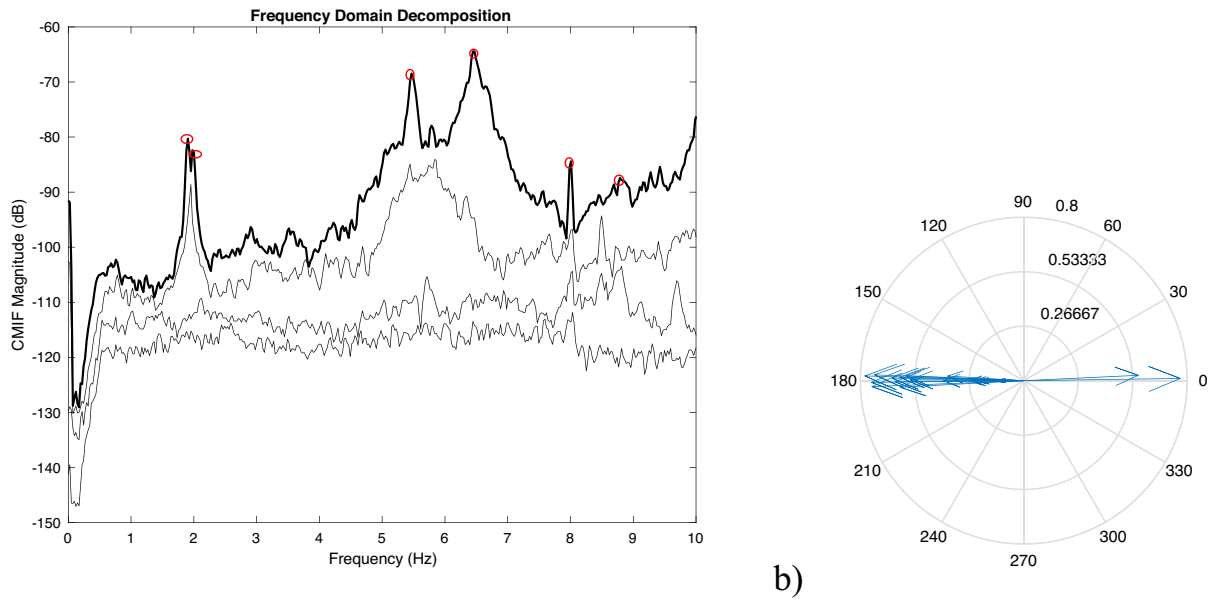
Fig. 7 **a** Example of envelope of singular value decomposition and peak picking (red circles); **b** example of compass plot of the 3rd mode shape

Table 1 Estimated frequencies

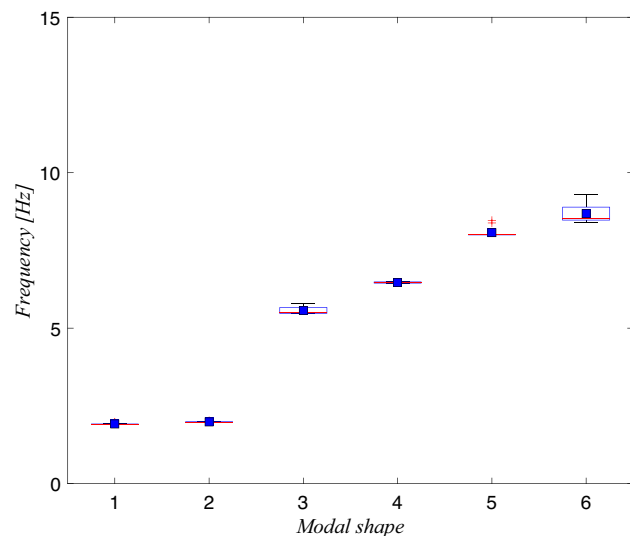| Mode	Frequency (Hz)		
	Mean	Median	Standard deviation
1	1.92	1.91	0.027
2	1.98	1.98	0.016
3	5.57	5.51	0.117
4	6.46	6.45	0.027
5	8.07	8.00	0.166
6	8.68	8.53	0.301

in the estimated frequencies, demonstrating the good accuracy of the selected peaks. The modal shapes obtained from the identification process are shown in Fig. 9. The focus was on the first two vibrational modes. Since no sensors could be placed in the upper part of the bell tower, the modal shapes were partially derived considering only the results of the lower levels. As can be seen in Fig. 9, the first four modes reflect modes of vibration that are compatible with a cantilevered structure such as the bell tower. The rotation of the mode shapes along the vertical axis of the tower is an aspect that will be specifically analysed in the following sections. In particular, the dependence between the non-pure bending in the two main planes and the crack extension is discussed. The fifth and sixth mode shapes did not appear to correspond to any physical mode; for this reason, they were subsequently excluded from the optimisation problem.

4 FE model updating

4.1 FE model

With the goal of developing a FE model that can be updated based on the OMA results and at the same time be the most efficient from a computational point of view, three different modelling approaches and FE models were developed. In the 1st model, beam-type elements were used and implemented in OpenSees software [19], in the 2nd and 3rd models, shell-type elements (Fig. 10) and brick-type were used in MidasGen software [20].
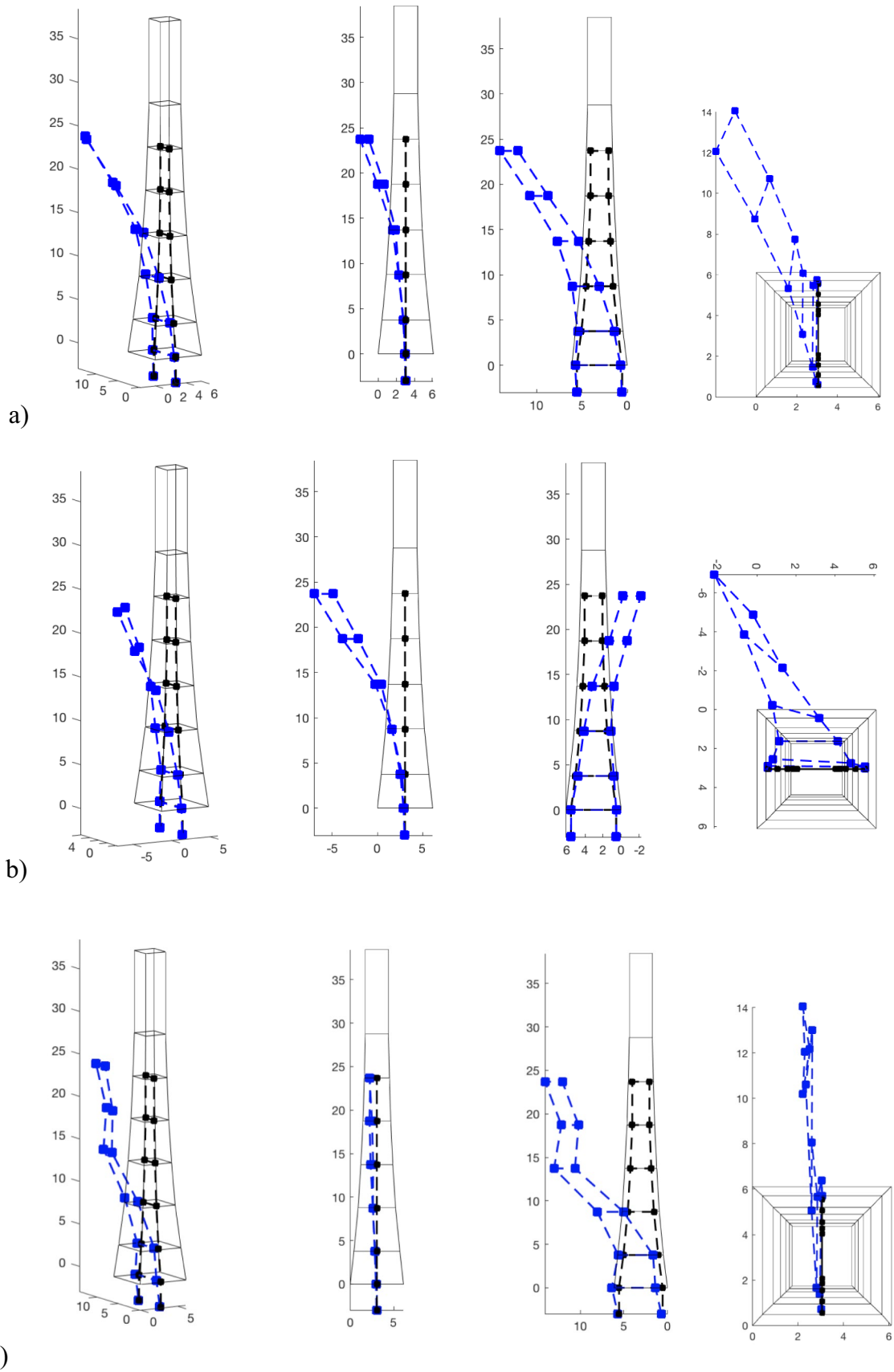

Fig. 8 Statistical distribution of the identified modal frequencies

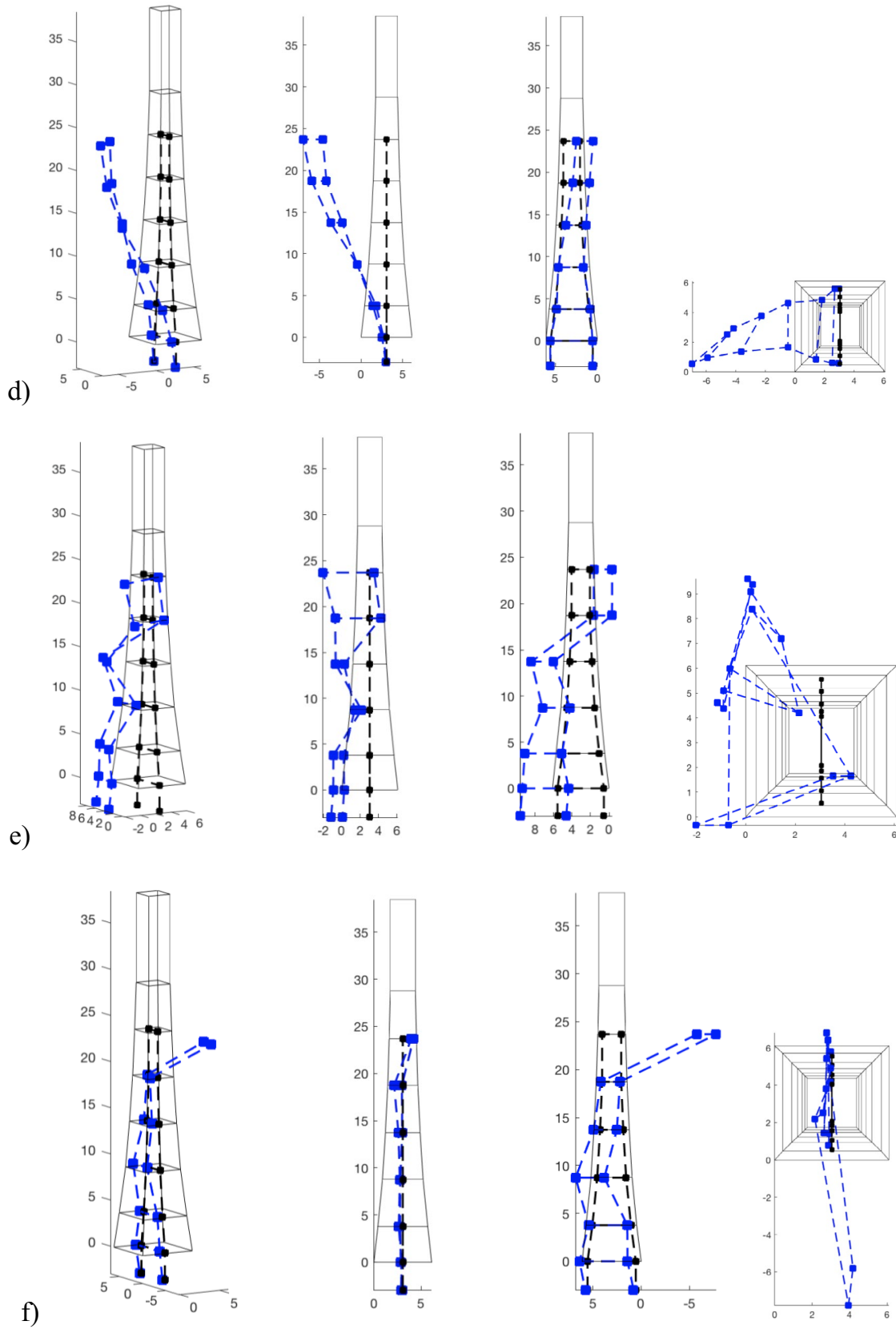**Fig. 9** 1st, 2nd, 3rd, 4th, 5th, and 6th mode shapes from OMA

Fig. 9 (continued)

Fig. 10 FE model with shell elements. *Note*: The model has 11,412 nodes and 20,516 elements for a total of 67,968 degrees of freedom

Table 2 Comparison between estimated and calculated frequencies before FE updating

Mode	Frequency (Hz)			
	OMA	Beam elements	Shell elements	Brick elements
1	1.92	2.63	2.61	2.60
2	1.98	2.94	2.92	2.89
3	5.57	8.89	7.10	6.92
4	6.46	11.12	8.85	8.35

While the brick model is the most accurate, the shell model requires less computational effort and agrees well with the results of the brick model. For this reason, the shell model was considered the best option to combine accuracy and computational efficiency.

Figure 12 shows the results of the modal assurance criterion (MAC) between the OMA and FE mode shapes before the update. The MAC value is the square of the correlation between two eigenvectors; if the index is 1, the compared vectors can be considered identical, otherwise if it is 0, they are to be considered different (orthogonal in the principal coordinates). From the results, the cross-correlations between modes 1&3 and 2&4 are quite high. This is partly because modes 1&3 and 2&4 have the same direction, and partly because the OMA modal shapes were only partially estimated with coarse resolution due to the lack of instrumentation in the upper part of the structure (Fig. 11). It is worth noting that six modes were identified in the ambient vibration tests, but only the first four modes were considered. In fact, the mode shapes extracted from peaks 5 and 6 (Fig. 9) were not considered in the objective function of the optimisation problem because they cannot be paired with the FE modes (Fig. 12).

4.2 Sensitivity analysis

Once the modal parameters were identified and an initial model was created, a sensitivity analysis was performed on certain model parameters that could potentially affect frequencies, modal shapes, and modal curvatures. In particular, the following parameters were selected: the elastic stiffnesses of the springs at the base, the percentage of crack damage (i.e., the scaling factor of the stiffness in the FE model), and the elastic modulus of the concrete (E_{cls}). Then, the tuning of these parameters was made considering the following considerations:

1. The modulus of elasticity of concrete has a significant effect on modal frequencies.
2. The damage in the cracked region (i.e., the stiffness scaling factor in the FE model) does not lead to significant
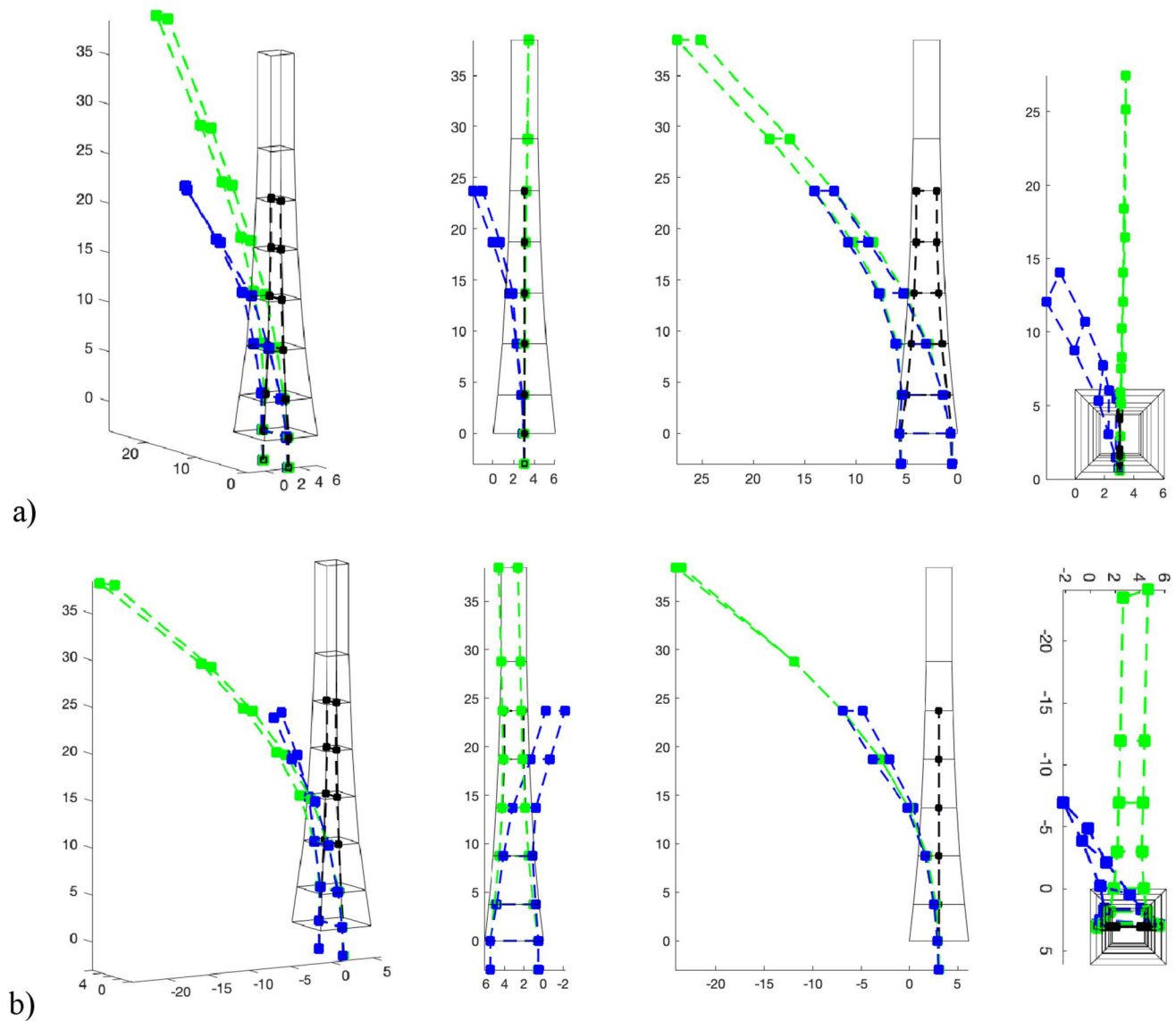
In all the FE models, two different thicknesses were used for the walls at each level to reproduce the cross-sectional shape of the tower as well as possible: in particular, 0.23 m and 0.32 m thick shell elements were used to model the thinnest and thickest areas (such as the corners), respectively. The belfry elements were 0.25 m thick, the floor slabs were 0.20 m thick, and a nodal mass of 2 kN/g was used to simulate the mass of the bells. To capture the soil–structure interaction, the shell elements were rigidly connected at the base to a fixed central node at which the rotational degrees of freedom in the x- and *y*-directions were removed and replaced by two elastic rotational springs.

The compressive strength of the concrete was selected based on the compression tests described in the previous section, while a conventional value was initially chosen for the modulus of elasticity, as the experimental data was not available. To simulate the crack in the 3rd level, a scaling factor for the stiffness was assigned to the shell elements in correspondence with the crack.

The 1st (beam-type elements) and the 2nd (shell-type elements) FE models were compared and differences in torsional mode shapes and higher vibration modes were found (Table 2). For this reason, and given the higher accuracy of the shell model, the 1st model with beam elements was not considered in the update of the FE model.

Another comparison was made between the 2nd (shell-type elements) and 3rd (brick-type elements) FE models.

Fig. 11 Comparison between 1st mode shape (**a**) and 2nd mode shape (**b**) before update: OMA (blue dashed line) and FE (green dashed line)

variations in terms of modal frequencies, but it does lead to a rotation of mode shapes along the vertical axis of the tower.

3. The stiffness of the rotational spring determines the modal curvature at the base.

Figure 13 shows the effect of the elastic modulus on the natural frequencies of the FE model. E_{cls} significantly affects the dynamic response of the structure: in general, the modal frequency increases when E_{cls} is increased. It is worth noting that the same elastic modulus was used for the entire structure. Figure 13 also shows the intersection between the FEM results and those of OMA. As expected, only one intersection was observed for each natural frequency.

Figure 14 shows how the first two modal shapes change depending on the extent of the crack on the 3rd level. Without the crack (black lines), the modal shapes are pure flexural modes in the *x* and *y* directions, while as the cracked area extends (red line), the modal shapes rotate about the vertical axis, as seen in Fig. 11.

The spring stiffness at the base affects both the modal frequency (Fig. 15) and the mode shapes (Fig. 16). As for the latter, the spring stiffness particularly affects the modal curvature at the base of the bell tower. It is worth noting that both the modal frequency and the mode shape do not change beyond a certain value of the spring stiffness.

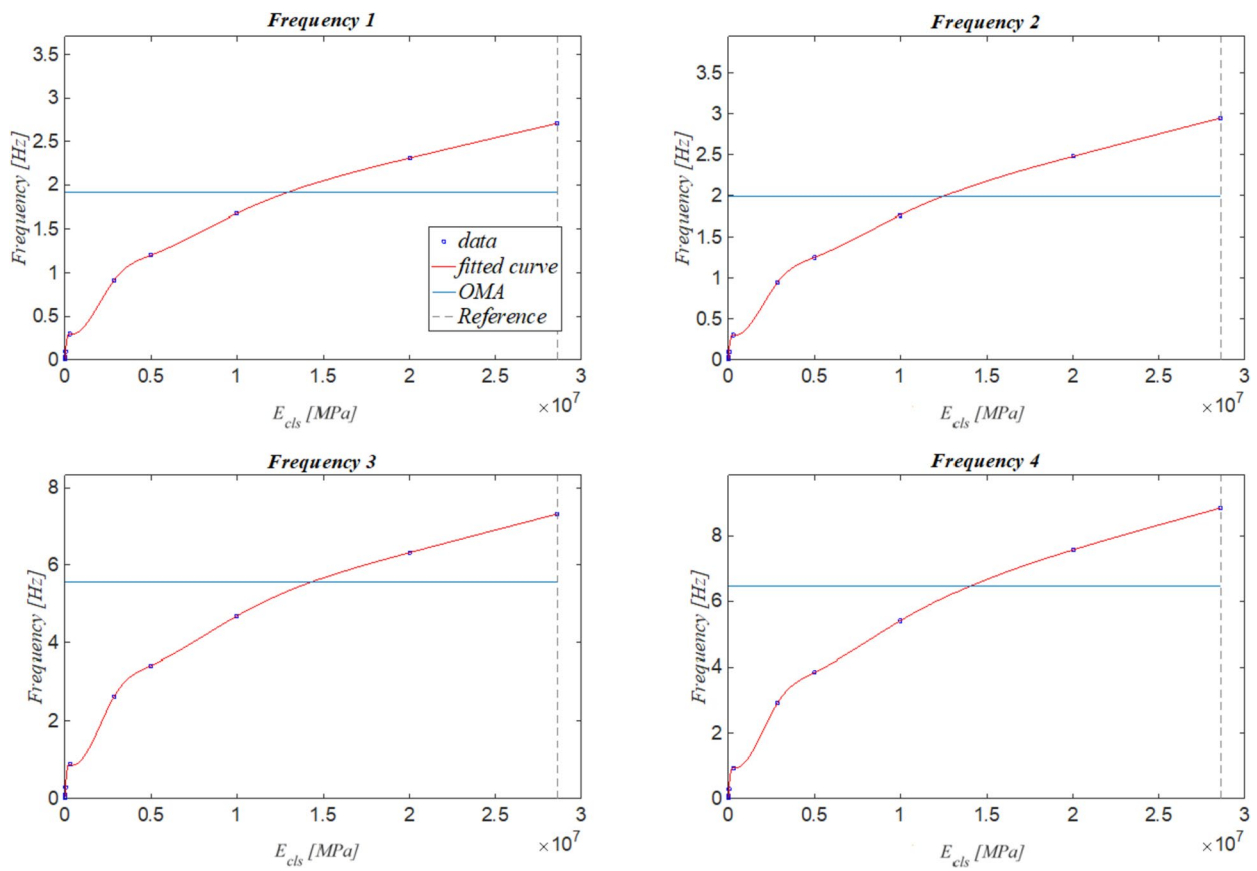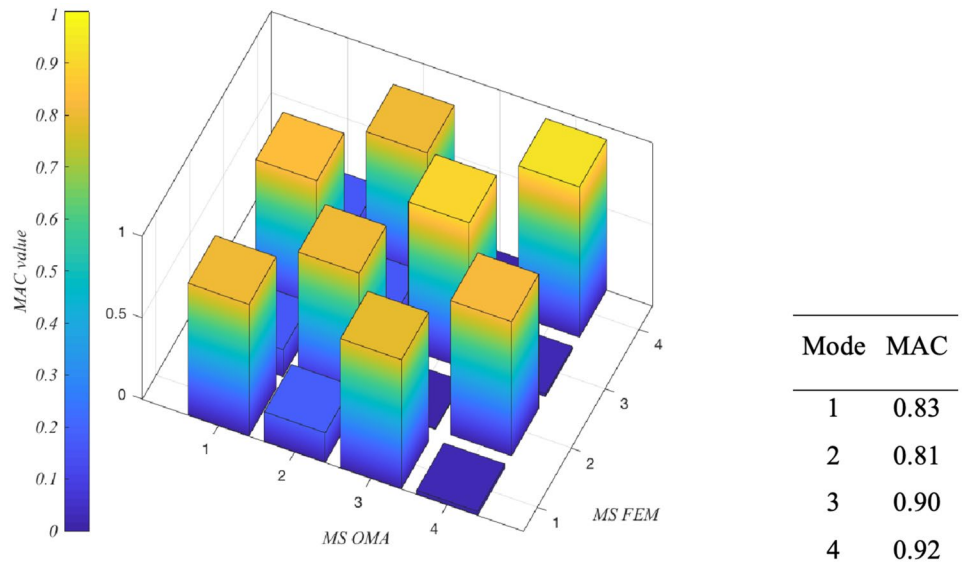**Fig. 12** MAC graph and values (OMA vs. FE) before update

Mode	MAC
1	0.83
2	0.81
3	0.90
4	0.92

Fig. 13 Sensitivity of the modal frequencies as a function of the modulus of elasticity of the concrete

4.3 Model parameter tuning

Based on the results of the sensitivity analysis, initial parameter tuning was performed by changing one parameter at a time. In particular, the base spring stiffness was set at 500,000,000 kNm/rad to obtain a curvature at the base of the first two mode shapes as similar as possible to the identified modal shapes. In this context, it is worth noting that the
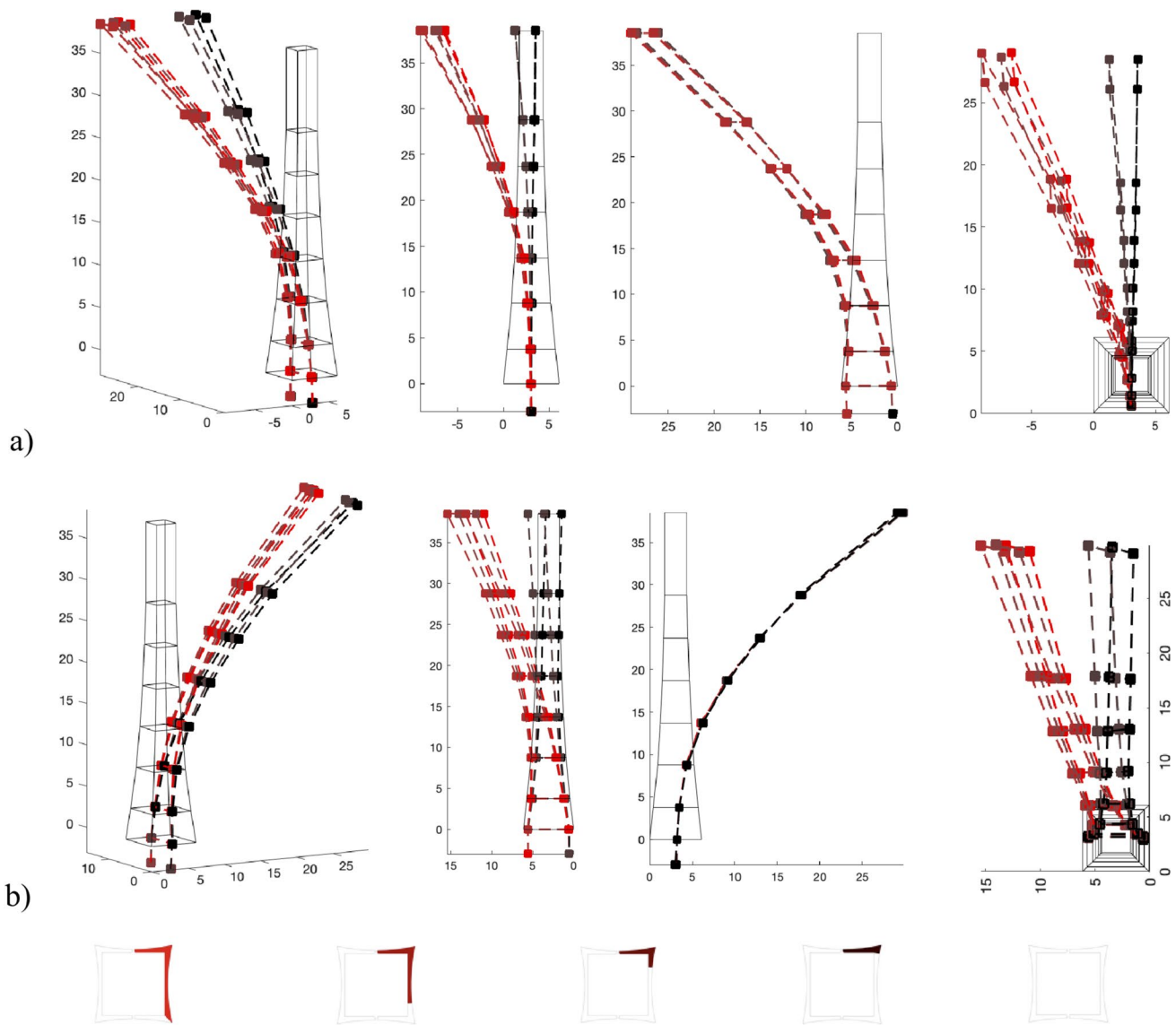
Fig. 14 Sensitivity of the 1st mode shape (**a**) and 2nd mode shape (**b**) as a function of the crack extension

results have shown that the tower can be considered practically fixed at the base; however, no geotechnical investigations were available that would have provided additional information.

The extent of the crack was tentatively set to 30% of the bell tower cross-section in the 3rd level. The modulus of elasticity of the finite elements belonging to the cracked region was significantly reduced (2% of the modulus of elasticity of the concrete) to consider the damage in this region. It was not possible to reduce it further to avoid numerical problems. The modulus of elasticity of the concrete was set at 28,600 MPa.

To obtain a more refined evaluation of the parameters, an objective function (F_{OB}) was defined considering the influence of the crack extensions (Cr in the Eq. 2) and

concrete modulus of elasticity (E in the Eq. 2). The latter was assumed constant in the whole tower:

$$F_{OB}(E, Cr) = \sum_{n=1}^{n° \text{ modes}} A \cdot \frac{1}{\alpha_n} \cdot \left(\frac{f_{OMA,n} - f_{FEM,n}(E, Cr)}{f_{OMA,n}} \right)^2 \\ + \sum_{n=1}^{n° \text{ modes}} B \cdot \frac{1}{\beta_n} \cdot \left(\frac{\theta_{OMA,n} - \theta_{FEM,n}(E, Cr)}{\theta_{OMA,n}} \right)^2 \quad (2)$$

Here, θ is the rotation of the mode shape around the vertical axis of the tower, α and β are the weights between the different modal frequencies and mode shapes (taken here as FE modal dynamic participation coefficient), while A and B are weights to broaden the importance of the frequencies to the mode shapes or vice versa. Part of the resulting objective
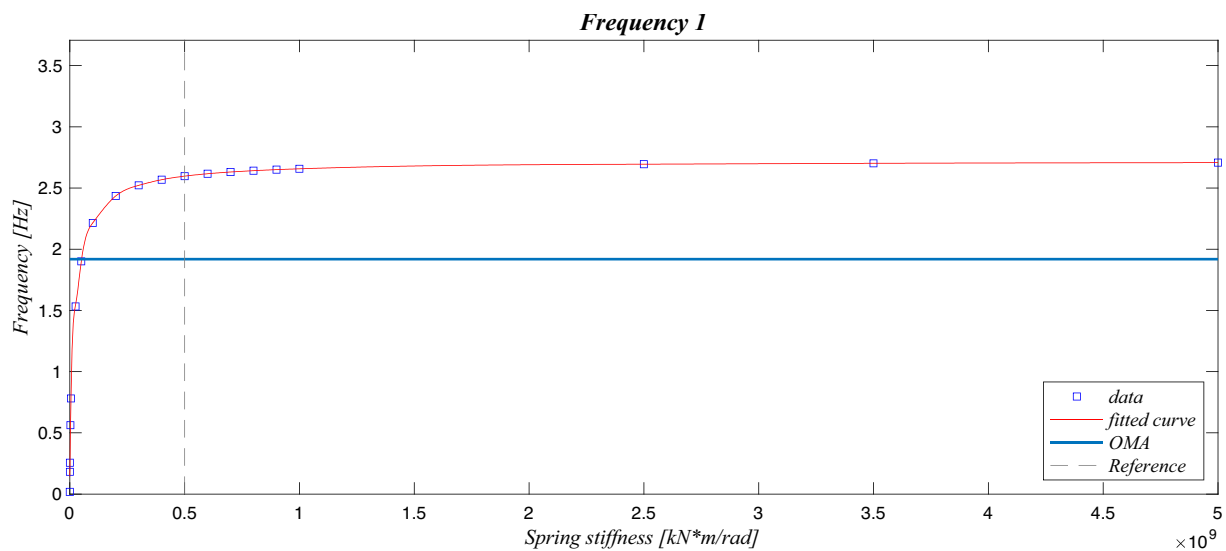
Fig. 15 Sensitivity of the 1st modal frequency as a function of the base spring rotational stiffness

function surface is shown in Fig. 17 as a function of crack extension and modulus of elasticity and for different weights.

When more weight is given to the modal frequencies (Fig. 17b), the damage extension becomes less sensitive, while the elastic modulus of the concrete becomes less sensitive when more weight is given to the modal shapes (Fig. 17c). It is interesting to note that the objective function in Fig. 17c has two minima. This can be explained by analysing the sensitivity analysis shown in Fig. 14: as the extent of damage increases, the rotation of the mode shape increases up to an extent of damage corresponding to half of the *C*-shape cross-section. With a subsequent increase in the damaged area, the rotation of the mode shape decreases, which leads to two minima of the objective function, i.e., to the unobservability of the inverse problem.

A global optimisation algorithm (function "fminsearch" in Matlab) was used to find the minimum value of the objective function. With this algorithm it is possible to find the global minimum with a good probability, even if there are several local minima. Since the standard algorithm for finding the global minimum has not been modified in any way, it has been listed in "Appendix 1". Figure 18 shows the function evaluation points through the entire Global Search Algorithm. The red mark highlights the global minimum. The algorithm refines the search in accordance with the two minimum points and finally finds the correct point.

In Table 3, the identified frequencies and the frequencies obtained from the model FE are superimposed before and after the optimization process. As expected, the FE frequencies of the initial model of the structure are higher (i.e., the undamaged structure is stiffer than the damaged one), while the frequencies obtained after the optimization process decrease, representing the damaged structure. The

effectiveness of the optimization process is also evident in Fig. 19, where the identified modal shapes overlap with those of the FE model. The effectiveness is also confirmed by the MAC values: 0.95, 0.96, 0.89, and 0.89, for the first four modal shapes, respectively.

5 Seismic assessment and retrofit

Modal identification and model updating were performed to calibrate and define the main parameters to be included in the FE model, such as the supports, elastic modulus, and crack extension. The updated and refined FE model was then used to develop and calibrate a new simplified model with beam-like elements using MidasGen software [20]. The simplified model consists of two vertical beam elements with a *C*-shaped cross-section with different thicknesses. In addition, the nonlinear behavior of concrete and steel was included in the updated FE model to evaluate the bell tower seismic safety. At each level, two beam elements have the same geometry of half of the bell tower cross-section (Fig. 20). The inelastic hysteresis of the vertical elements was accounted for by lumped plastic hinges capturing the flexural behavior with a degrading tetralinear Takeda constitutive law [21]. More precisely, the flexural plastic hinge is a trilinear curve followed by a degrading branch whose characteristic points were calculated based on the formulations proposed in the Eurocodes [22] and considering the available structural details (see "Appendix 2"). A 0.20 m thick beam element resembling the existing floor slab was used to connect the two *C*-shaped vertical elements (Fig. 20b). A plastic hinge was introduced at mid-span of the connecting horizontal beam and calibrated according to the capacity
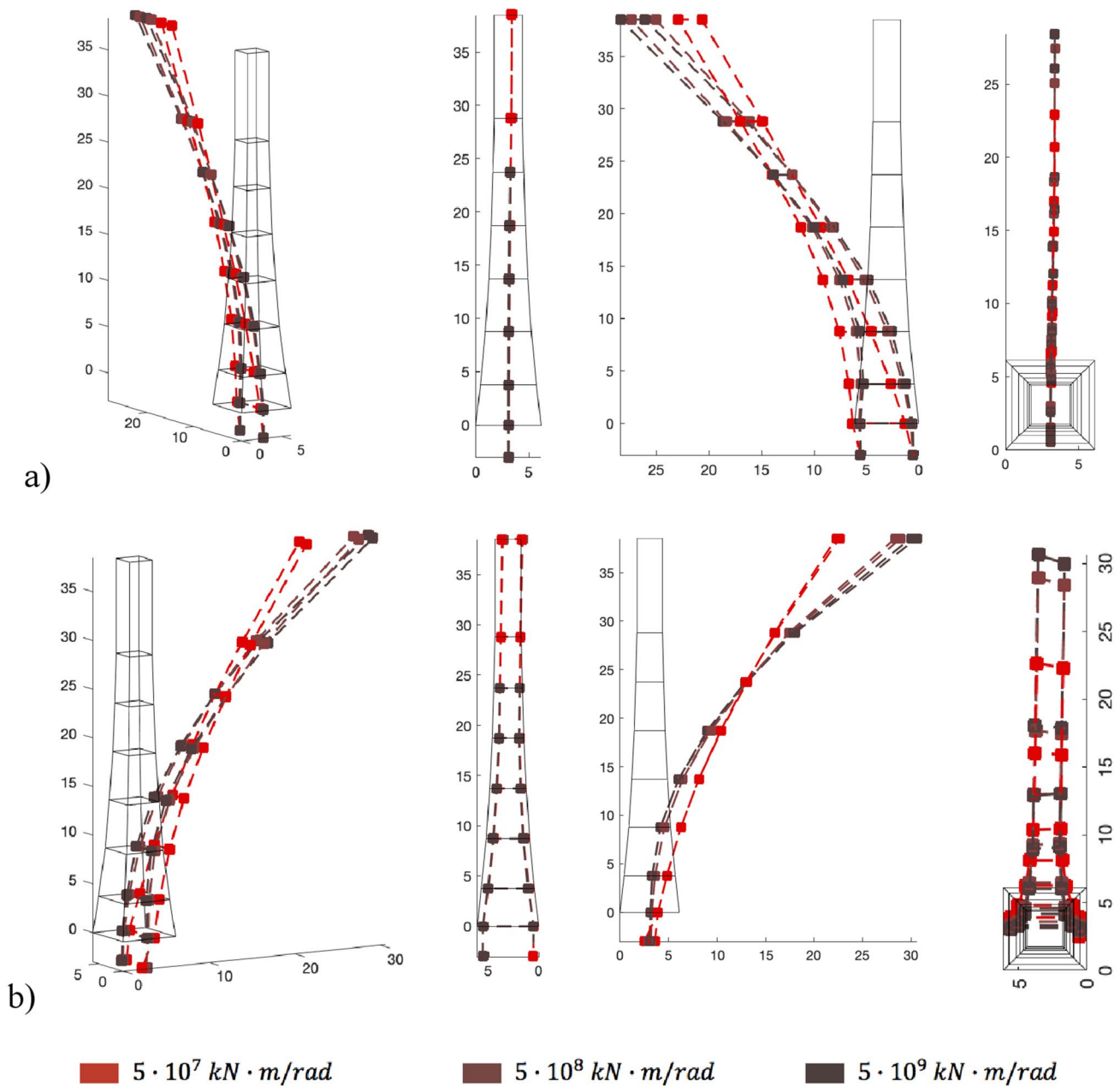
Fig. 16 Sensitivity of the 1st mode shape (**a**) and 2nd mode shape (**b**) as a function of as the base spring rotational stiffness

of the existing RC slab. To validate the simplified beam model in the elastic domain, a modal analysis was performed and the results were compared with those of the shell-type model, which showed good agreement (1st and 2nd mode frequencies equal to 1.92 Hz and 2.00 Hz, respectively). Once the nonlinear FE model was defined, a seismic vulnerability assessment was performed using nonlinear static (pushover) analysis according to the current building codes. The flowchart of the entire applied framework is shown in Fig. 21.

The analyses were performed considering both uniform and first-mode proportional lateral load distributions. In the *x*-direction, the main weak point was identified at the vertical discontinuity in the facades where the coupling beam resembling the RC slab was placed (Fig. 20b): in these areas, due to the horizontal external loads, there is a concentration of forces due to the coupling of the two parts of the bell tower through the floor slab RC. In the *x*-direction, no differences were observed between the positive and negative directions due to the symmetry of the structure. In the *y*-direction, the negative direction (−y)
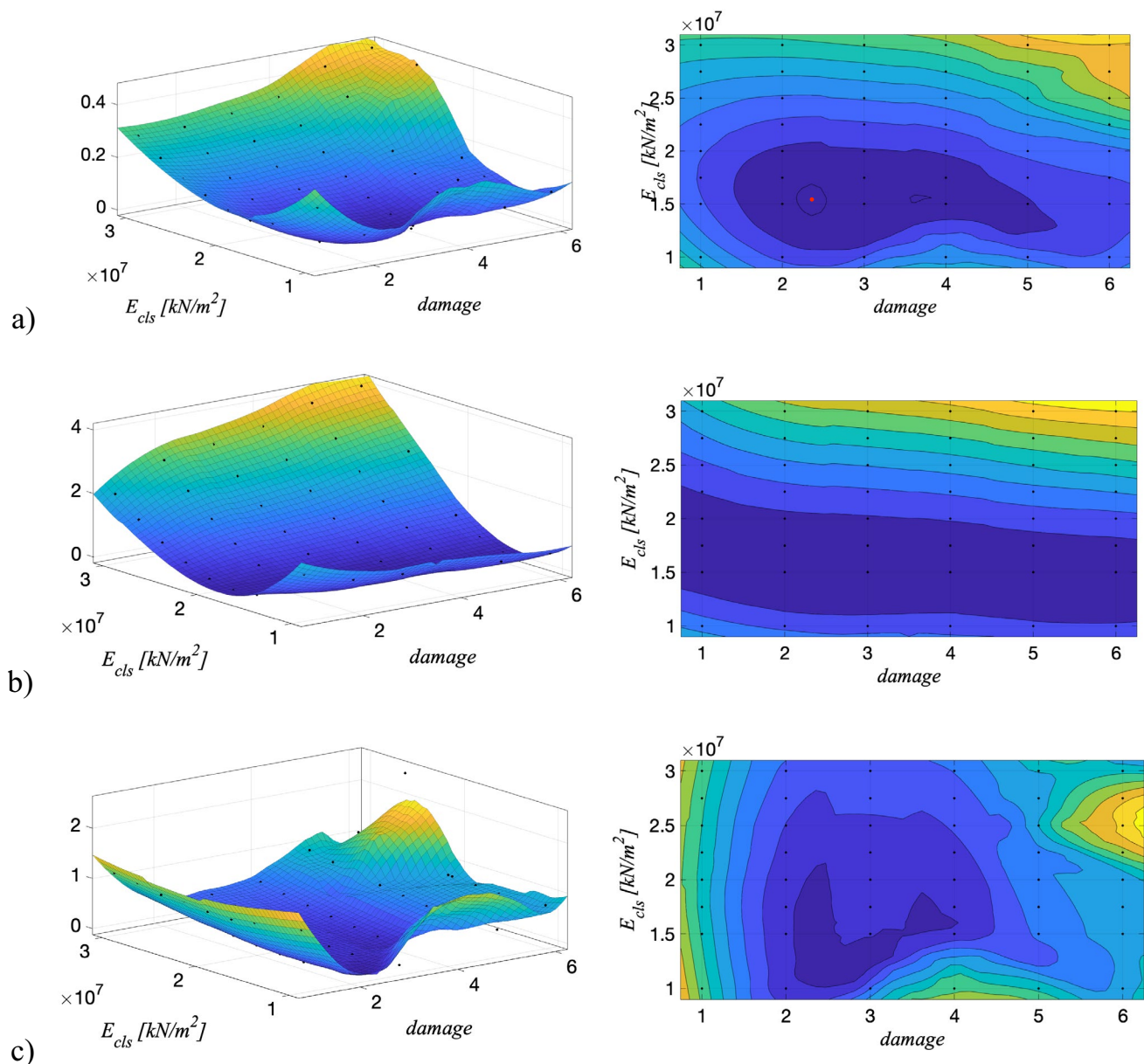
Fig. 17 Objective functions with different weights: **a** same weights between modal frequencies and mode shapes; **b** higher weights for modal frequencies than mode shapes; **c** higher weights for mode shapes than modal frequencies

was the most vulnerable due to the asymmetry caused by the crack in the 3rd level, and the main vulnerability was related to the horizontal crack in the 3rd level.

Figure 22 shows the results of the nonlinear static assessment of the seismic vulnerability in the *x*- and *y*-directions, plotted in the acceleration–displacement response spectrum (ADRS). The results are based on a nominal life of 100 years, a ground acceleration of 0.144 g at the Life Safety Limit State (LSLS), a soil category B, and T1 topography [23].

The ultimate displacement corresponds to the failure of the RC slab across the vertical discontinuity in the cross-section of the bell tower, *x*-direction (Fig. 22a), and to the activation of the plastic hinge at the cracked 3rd level, *y*-direction (Fig. 22b). The LSLS and Collapse Prevention Limit State (CPLS) were defined based on the rotation reached in the lumped plastic hinges; in particular, the CPLS was set according to the ultimate rotational capacity of the flexural plastic hinges while LSLS limit was considered to be reached at 3/4 of such rotation capacity [23]. In the *y*-direction, since the activation of the plastic hinges representing the crack occurred earlier than the LSLS requirement, a structural retrofit was considered.

Fig. 18 Tentative points of the global search algorithm
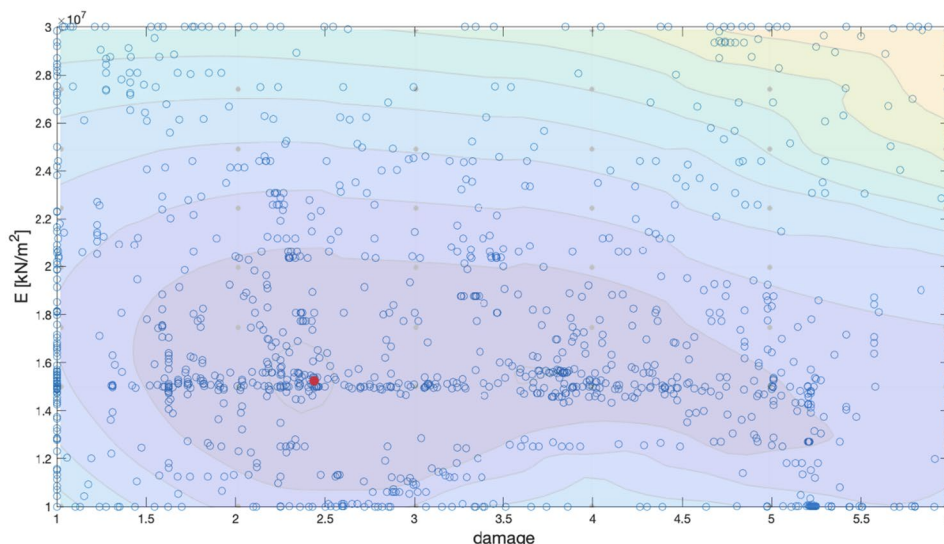

Table 3 Comparison between estimated and calculated frequencies before FE updating

Mode	OMA	FE-before	FE-after
1	1.92	2.61	1.92
2	1.98	2.92	2.13
3	5.57	7.10	5.68
4	6.46	8.85	6.62

The retrofit intervention was proposed considering that the main seismic vulnerability is represented by the cracked region at the 3rd level and that in undamaged conditions, the bell tower would be able to withstand the design-basis earthquake. A local retrofit intervention was therefore selected by restoring the damaged concrete with thixotropic mortar of class R4, and by providing post-tensioning force, to first achieve a normal stress at the retrofitted area compatible with the one in the undamaged conditions under gravity loads (Step 1), and then, to keep the damaged area compressed in the case of the LSLS Earthquake (Step 2). In both cases, the seismic vulnerability assessment was carried out.

From a technological point of view, the proposed intervention was conceived as a set of two double S275 UPN160 profiles ($L = 0.52$ m and 30 mm spaced) placed in pockets made in the walls of the bell tower, above and below the upper and lower decks close to the corners of the cracked façade (Fig. 23a, b). The double UPN, 32 mm spaced, allows the positioning of a ϕ28 mm post-tensioning bar (Fig. 23c); as for Step 1 and Step 2, 224 kN and 616 kN are considered. It is worth noting that the stress increase which arises in the bell tower walls due to post-tensioning is negligible compared to the wall axial capacity.

From the FE analysis point of view, the retrofitted area was modelled by replacing the plastic hinge introduced to model the damaged area with a new plastic hinge whose moment-rotation hysteresis was calibrated according to the applied post-tensioning. As in step 1, the preload was derived by considering a vertical load of 890 kN on the *C*-shaped element. The CPLS was determined at the activation of the plastic hinge in the damaged region (i.e., when the value of the post-tension was reached and a tensile stress state occurred in the damaged region); at the end of Step 1, a seismic safety index of 0.75 was obtained (Fig. 24).

In Step 2, the tensile stress that would develop in the 3rd level due to the overturning moment was evaluated and the prestressing was designed accordingly. A tensile force of 513 kN was determined in the cracked area. By multiplying this value by a safety factor of 1.20, the preload was defined and the plastic hinge hysteresis was calibrated. The capacity curve of the retrofitted bell tower along the *y*-direction is shown in Fig. 24. The intervention allows engaging a distributed plastic region along the bell tower height, the yield strength and ultimate strength of the plastic hinge are reached at the 4th level, respectively. A seismic safety index greater than 1 was obtained.

6 Summary and conclusion

The paper presents the system identification, the assessment of the extent of damage through a global optimisation algorithm, the evaluation of the seismic vulnerability and the proposal for the retrofitting of the RC bell tower of the
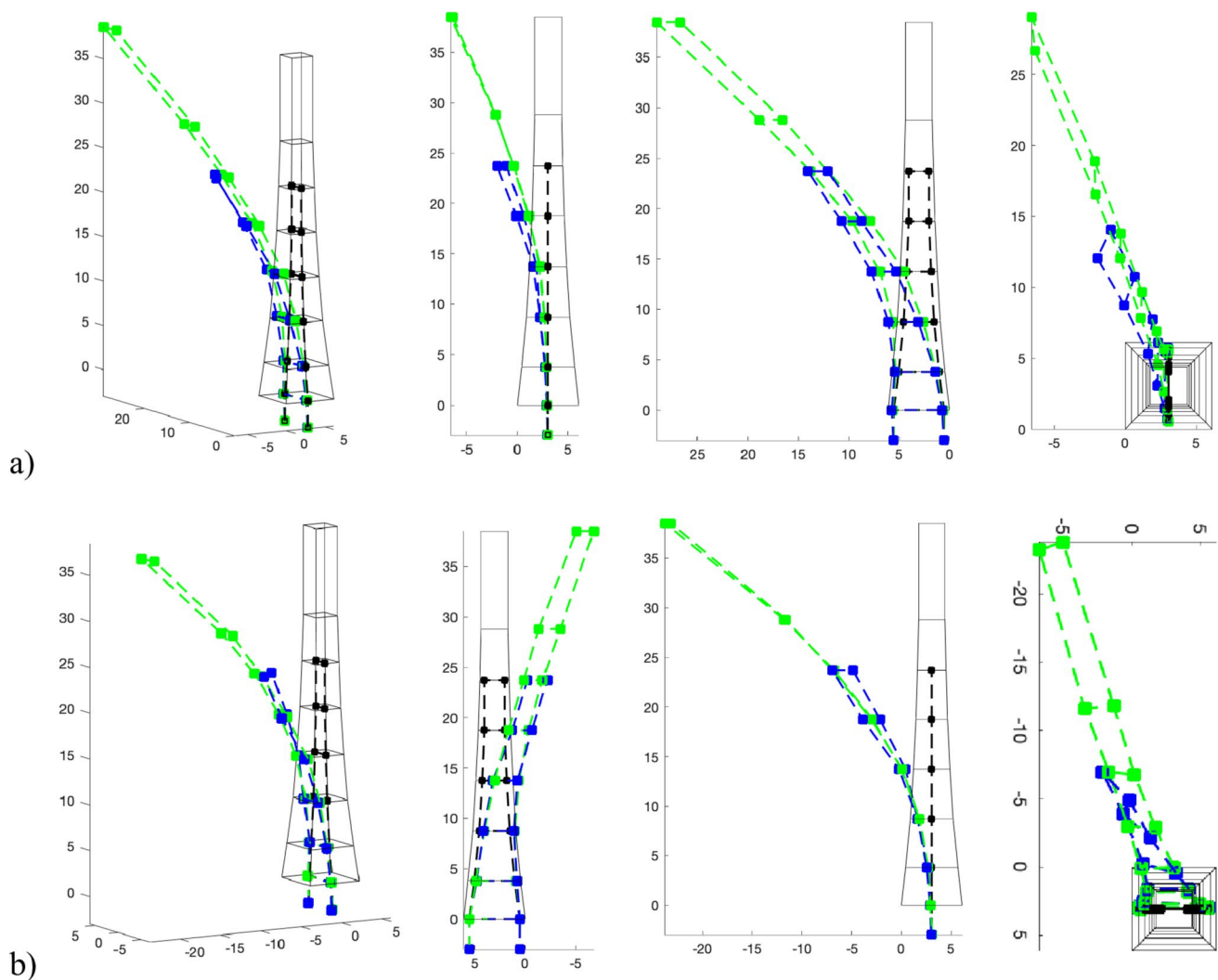
Fig. 19 Comparison between 1st mode shape (**a**) and 2nd mode shape (**b**) after update: OMA (blue dashed line) and FE (green dashed line)

church of San Giacomo in the municipality of Castro (Italy). The tower was severely damaged by a continuous crack in the 3rd level and advanced corrosion of the reinforcing bars passing through the crack. A modal identification was carried out with a small number of sensors measuring the environmental vibrations (Operational Modal Analysis—OMA). A roving method was used to capture the mode shapes with adequate spatial resolution despite the small number of sensors. The frequency domain decomposition algorithm was applied to each data set and then combined to obtain the full model mode shapes.

The extent of damage in the cracked region on the 3rd level was assessed by a global optimisation algorithm. To obtain a reliable FE model for damage detection, two types of FE models were first developed, namely a beam-type model and a shell-type model. The former resulted in a less accurate model, especially in terms of the torsional

component, so the more accurate shell element model was chosen to update the FE model.

A sensitivity analysis was carried out to show the influence of the various mechanical and geometric parameters on the dynamic properties of the bell tower. In particular, it was found that the extent of damage in the cracked region at the 3rd level induces a rotation of the modal shapes around the vertical axis, which is compatible with the OMA results; the stiffness of the rotational springs at the base of the model can be chosen to match the modal curvature at the base of the tower; the modulus of elasticity of the concrete significantly affects the modal frequencies. Initially, several model parameters were manually adjusted to achieve a generally good agreement with the identified dynamic properties of the OMA and to quantify the damage in the cracked region. The determined values of the model parameters served as
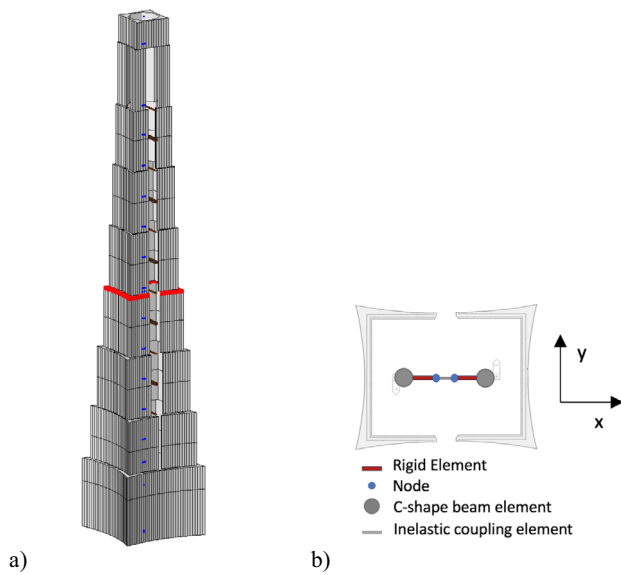
Fig. 20 Simplified beam-like finite element model (**a**) with the crack position in red, and cross-section (**b**)

a starting point for a global optimisation algorithm, which made it possible to find the best values for updating the parameters. These were defined as the extent of the through-crack in the cross-section in the 3rd level and the modulus of elasticity of the concrete.

The updated model was used as a benchmark to define the elastic properties of a nonlinear beam model, with which an assessment of the seismic vulnerability of the bell tower was carried out, showing the low capacity of the bell tower in one direction due to the damaged area on the 3rd level. Finally, based on the seismic vulnerability results, a possible local retrofit intervention was proposed, replacing the concrete in the damaged region with a thixotropic mortar and creating an active normal stress in the repaired region with prestressing bars.

Appendix 1

The considered algorithm for finding the global minimum consists of the following steps:

- Run the local minimum search algorithm from a given starting point and, if it converges, plot the optimization path for the next points.
- Use a scatter search algorithm to generate a set of test points within the search area. Such points are possible starting points.

- Evaluate the function in the test points and run the algorithm to find the local minimum from the best of these points (Stage 1).
- At this point, the solution points are the points found starting from the starting point and the points of Stage 1. The heuristic hypothesis predicts that the valleys of the function are spherical, whose radii are calculated as the distance between the solution point and the starting point.
- Loop the remaining test points until certain conditions are met.
- After considering all test points or reaching the maximum time allowed, create the solution vector, sorted by the lowest (best) and the highest (worst) value of the objective function.

The approach used to solve the constrained optimization problem is to solve a set of approximation problems [24]. The initial problem is:

$$\min_{x} f(x), \quad \text{subject to} \quad h(x) = 0 \quad \text{and} \quad g(x) \leq 0 \tag{3}$$

For each $\mu > 0$ the problem is approximated as follows:

$$\begin{aligned} &\min_{x,s} f_\mu(x, s) \\ &= \min_{x,s} f(x) - \mu \sum_i \ln(s_i), \quad \text{subject to} \quad s \geq 0, \\ &h(x) = 0 \quad \text{and} \quad g + s = 0 \end{aligned} \tag{4}$$

where there are as many variables s_i as constraints g.

The logarithmic term is commonly referred to as the barrier function [25, 26]. To solve the problem described in Eqs. 3 and 4, the algorithm uses one of the following two principles: "direct step" and "conjugate gradient".

Direct step: in this case, an attempt is made to solve the approximated problem (Eq. 4) through a further linear approximation.

The process is summarized below.

- H denotes the Hessian matrix of the Langrage function of f_u

$$H = \nabla^2 f(x) + \sum_i \lambda_i \nabla^2 g_i(x) + \sum_i y_j \nabla^2 h_j(x) \tag{5}$$

- J_g is the Jacobian of the constraint function g.
- J_h is the Jacobian of the constraint function h
- $S = \text{diag}(s)$
- λ are the Lagrange multipliers for the constraints g
- $\Lambda = \text{diag}(\lambda)$
- y are the Lagrange multipliers for h
- e is a vector of zero of the same size as g.

Fig. 21 Flowchart showing the various steps of the entire followed framework
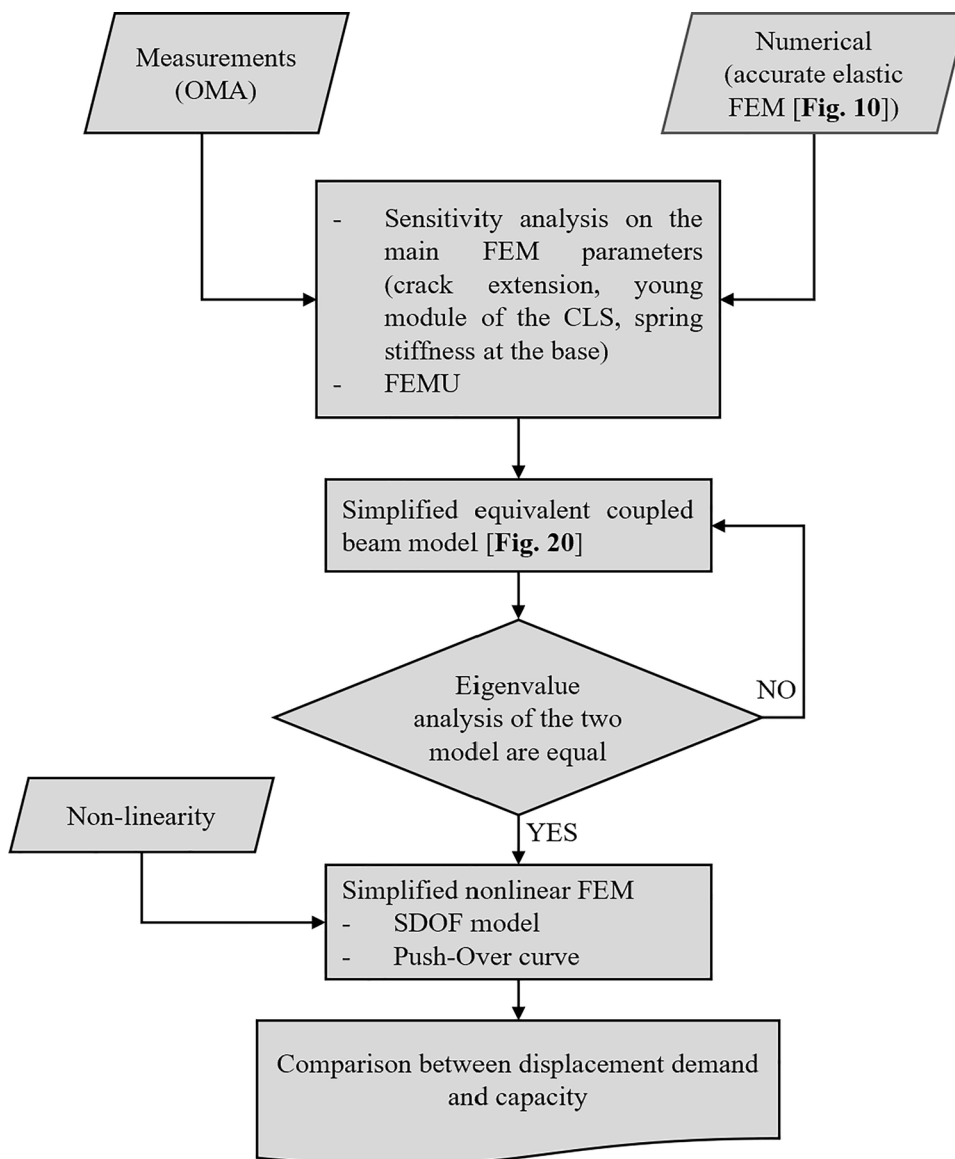
Resolution via direct step takes place via

$$
\begin{bmatrix} H & 0 & J_h^T & J_s^T \\ 0 & \Lambda & 0 & S \\ J_h & 0 & 0 & 0 \\ J_g & I & 0 & 0 \end{bmatrix} \begin{bmatrix} \Delta x \\ \Delta s \\ \Delta y \\ \Delta \lambda \end{bmatrix} = - \begin{bmatrix} \nabla f + J_h^T y + J_s^T \lambda \\ S\lambda - \mu e \\ h \\ g + s \end{bmatrix} \quad (6)
$$

For its resolution, the algorithm uses an LDL factorization. This factorization allows to determine the definition of the Hessian matrix. If the matrix is not positive defined, the algorithm passes to a resolution through a conjugate gradient.

Conjugate gradient

The approach in this case consists in minimizing a quadratic approximation of the problem in a confidence region subject to linearized constraints.

The algorithm tries, as a first approach, the resolution through *Direct step*. If it fails, then it tries again via *Conjugated Gradient*.
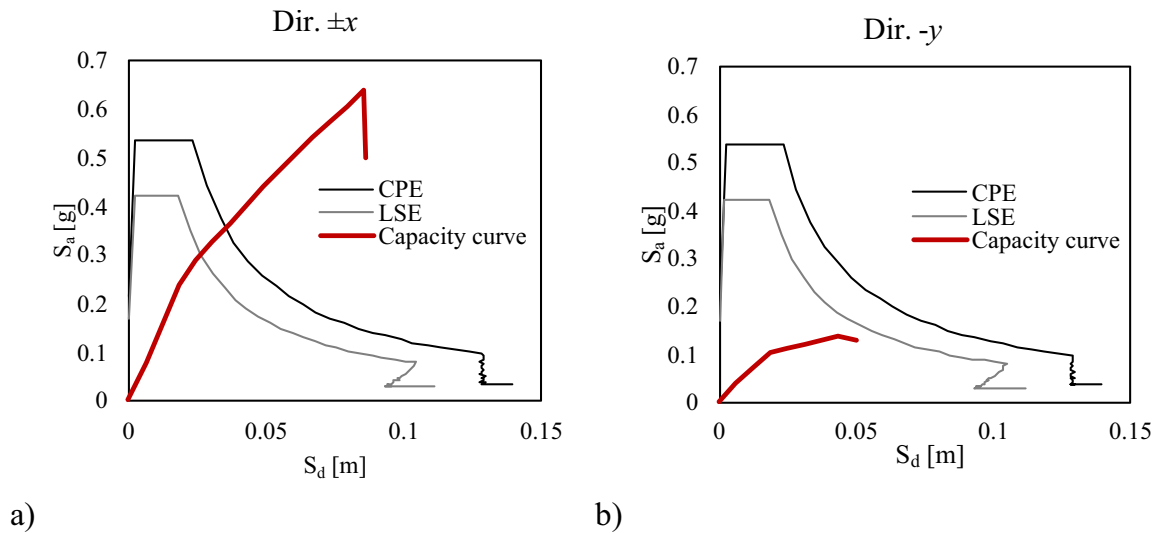
Fig. 22 Capacity spectrum of the bell tower in the AS-IS conditions: direction *x* (**a**), and *y* (**b**). *Note*: LSE is the life safety earthquake; CPE is the collapse prevention earthquake

Appendix 2

The values of the degrading tetralinear Takeda plastic hinges included in the model are summarized below. A symmetrical behavior was considered for the plastic flexural hinges used in the undamaged *C*-shaped beam element. M_y and M_z refer to the local axes of the element, which correspond to the global axes *Y* and *X* in Fig. 2.

Ground level (PT)				Level 4 (P4)			
M_y		M_z		M_y		M_z	
kNm	rad/m	kNm	rad/m	kNm	rad/m	kNm	rad/m
48,560	0.00037	48,560	0.00037	1039	0.00175	1048	0.00003
62,060	0.00338	62,060	0.00338	1040	0.00176	1644	0.00064
63,740	0.00538	63,740	0.00538	1147	0.00628	1841	0.01579
42,701	0.0056	42,701	0.0056	1	0.007	503	0.016

Level 1 (P1)				Level 5 (P5)			
M_y		M_z		M_y		M_z	
kNm	rad/m	kNm	rad/m	kNm	rad/m	kNm	rad/m
3609	0.00110	3703	0.00002	730	0.00188	738	0.00004
3945	0.00669	5437	0.00042	813	0.01580	1131	0.00073
4062	0.01289	6237	0.00787	813	0.03221	1266	0.02032
1267	0.023	1412	0.008	534	0.037	308	0.021

Level 2 (P2)				Level 6 (P6)			
M_y		M_z		M_y		M_z	
kNm	rad/m	kNm	rad/m	kNm	rad/m	kNm	rad/m
2791	0.00143	2468	0.00002	507	0.00211	820	0.00084
3040	0.00667	4271	0.00052	571	0.01821	961	0.01894
3097	0.01325	4454	0.00787	589	0.03744	961	0.02655
1928	0.016	1078	0.008	380	0.048	279	0.028

Level 3 (P3)			
M_y		M_z	
kNm	rad/m	kNm	rad/m
1629	0.00159	1785	0.00007
1804	0.00899	2528	0.00061
1845	0.01888	2872	0.01263
1095	0.023	810	0.013

An asymmetric behavior was introduced to simulate the crack at the 3rd level (P3).

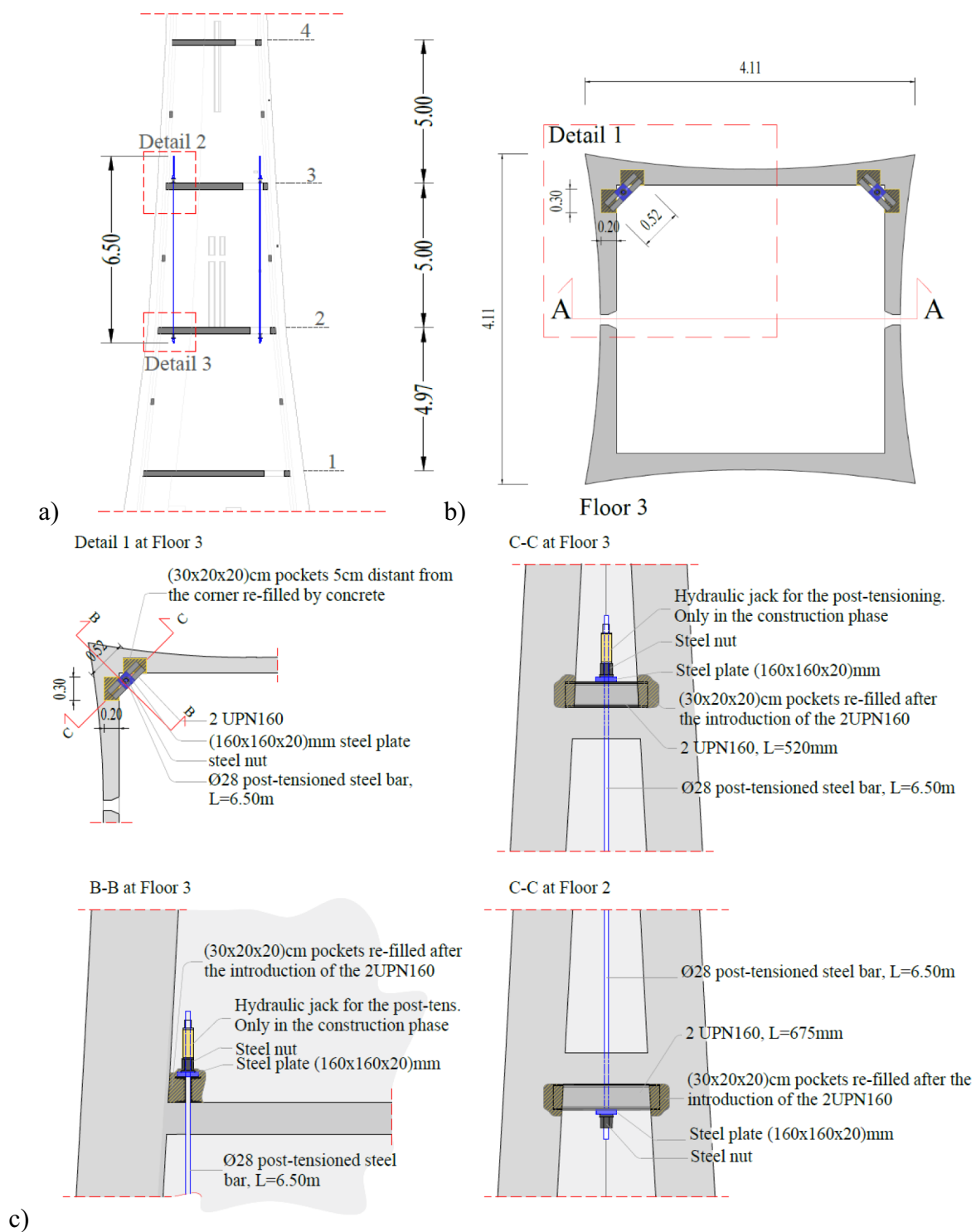| Cracked P3: Left *C*-shape element							
M_y				M_z			
kNm		rad/m		kNm		rad/m	
(+)	(−)	(+)	(−)	(+)	(−)	(+)	(−)
1333	513	0.00169	0.00125	574	1429	0.00114	0.00151
1405	617	0.03175	0.00745	674	1522	0.00739	0.00327
1459	650	0.01140	0.02326	703	1572	0.02321	0.01214

Fig. 23 Drawings of the proposed local retrofit intervention: **a** vertical section and position of the retrofit intervention; **b** cross-section at the 3rd level; **c** details and description of the retrofit intervention
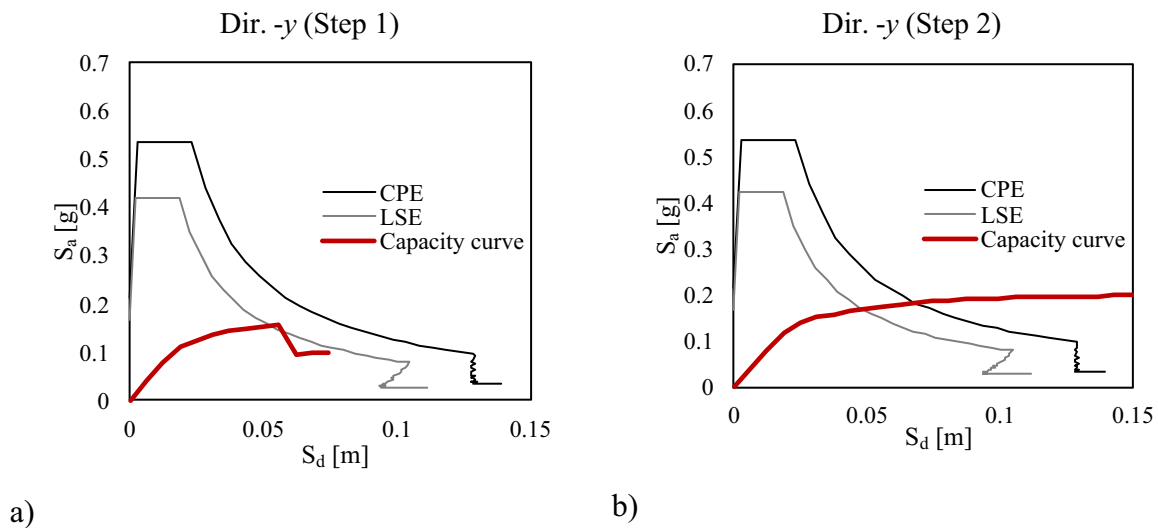
Fig. 24 Capacity spectrum of the retrofitted bell tower in the weakest direction (negative y-direction): **a** Step 1; **b** Step 2

Cracked P3: Left C-shape element

M_y				M_z			
kNm		rad/m		kNm		rad/m	
(+)	(−)	(+)	(−)	(+)	(−)	(+)	(−)
206	566	0.018	0.05779	625	1	0.05286	0.02

Cracked P3: Right C-shape element

M_y				M_z			
kNm		rad/m		kNm		rad/m	
(+)	(−)	(+)	(−)	(+)	(−)	(+)	(−)
425	1561	0.001216	0.00178	1488	2753	0.00063	0.00069
554	1635	0.00932	0.00297	1713	3003	0.00714	0.00241
582	1697	0.02966	0.01094	1771	3118	0.02243	0.00805
561	1	0.05086	0.02	1685	1	0.02533	0.017

References

1. ASCE Technical Committee on Structural Identification (2013) Structural identification of constructed systems: approaches, methods, and technologies for effective practice of St-Id. In: Çatbas, FN, Kijewski-Correa T, Aktan AE (eds) ASCE
2. Belleri A, Moaveni B, Restrepo JI (2014) Damage assessment through structural identification of three-story large-scale precast concrete structure. Earthq Eng Struct Dyn 2014:1
3. Carden EP, Fanning P (2004) Vibration based condition monitoring: a review. Struct Health Monit 3(4):355–377
4. Doebling SW, Farrar CR, Prime MB (1998) A summary review of vibration-based damage identification methods. Shock Vib Digest 30(2):99–105
5. Fan W, Qiao P (2011) Vibration-based damage identification methods: a review and comparative study. Struct Health Monit 10(1):83–111
6. Farrar CR, Worden K (2007) An introduction to structural health monitoring. Phil Trans R Soc A 365:303–315
7. Friswell MI, Mottershead JE (2010) Finite element model updating in structural dynamics. Springer, Dordrecht
8. Lam H-F, Hu J, Yang J-H (2017) Bayesian operational modal analysis and Markov chain Monte Carlo-based model updating of a factory building. Eng Struct 132:314–336

9. Moaveni B, Stavridis A, Lombaert G, Conte JP, Shing B (2013) Finite-element model updating for assessment of progressive damage in a 3-story infilled RC frame. J Struct Eng 2013:1

10. Ozcelik O, Misir IS, Yucel U, Durmazgezer E, Yucel G, Amaddeo C (2022) Model updating of Masonry courtyard walls of the historical Isabey mosque using ambient vibration measurements. J Civil Struct Health Monit 12:1157–1172

11. Sohn H, Farrar CR, Hemez FM, Shunk DD, Stinemates DW, Nadler BR (2003) A review of structural health monitoring literature: 1996–2001. Technical report, Los Alamos National Laboratory, LA-13976-MS, Los Alamos, New Mexico, USA

12. Thibault L, Marinone T, Avitabile P, Van Karsen C (2012) Comparison of modal parameters estimated from operational and experimental modal analysis approaches. In: Allemang R, De Clerck J, Niezrecki C, Blough J (eds) Topics in modal analysis I, volume 5. Conference proceedings of the society for experimental mechanics series. Springer, New York

13. Zhu Y-C, Xie Y-L, Au S-K (2018) Operational modal analysis of an eight-storey building with asynchronous data incorporating multiple setups. Eng Struct 165:50–62

14. Benedettini F, Gentile C (2011) Operational modal testing and FE model tuning of a cable-stayed bridge. Eng Struct 2011:1

15. Cardoso R, Cury A, Barbosa F (2017) A robust methodology for modal parameters estimation applied to SHM. Mech Syst Signal Process 2017:1

16. Ubertini F, Gentile C, Materazzi AL (2013) Automated modal identification and its application to bridges. Eng Struct 2013:1

17. UNI 9916:2004. Criteri di misura e valutazione degli effetti delle vibrazioni sugli edifici

18. Brincker R, Zhang L, Andersen P (2000) Modal identification of output-only systems using frequency domain decomposition. Smart Mater Struct 10(3):441

19. McKenna F (2011) OpenSees: a framework for earthquake engineering simulation. Comput Sci Eng 13(4):58–66

20. MidasGEN 2020 (v2.1), MIDAS Information Technologies Co. Ltd.

21. Otani S (1974) SAKE: a computer program for inelastic response of R/C frames to earthquakes

22. EC8 (2005) Design of structures for earthquake resistance. European Committee for Standardization, CEN, Brussels, Belgium

23. NTC (2018) Norme Tecniche per le Costruzioni (NTC 2018), Gazzetta Ufficiale del 20/02/2018, Supplemento ordinario n. 42

24. Byrd RH, Gilbert JC, Nocedal J (2000) A trust region method based on interior point techniques for nonlinear programming. Math Program 89(1):149–185

25. Byrd RH, Hribar ME, Nocedal J (1999) An interior point algorithm for large-scale nonlinear programming. SIAM J Optim 9(4):877–900

26. Waltz RA, Morales JL, Nocedal J, Orban D (2006) An interior algorithm for nonlinear optimization that combines line search and trust region steps. Math Program 107(3):391–408